



In situ spectral measurements of space weathering by Chang'e-4 rover

Sheng Gou^{a,b}, Zongyu Yue^{a,c}, Kaichang Di^{a,b,c,*}, Wenhui Wan^a, Zhaoqin Liu^a, Bin Liu^{a,b}, Man Peng^a, Yexin Wang^a, Zhiping He^d, Rui Xu^d

^a State Key Laboratory of Remote Sensing Science, Aerospace Information Research Institute, Chinese Academy of Sciences, Beijing 100101, China

^b State Key Laboratory of Lunar and Planetary Sciences, Macau University of Science and Technology, Macau, China

^c CAS Center for Excellence in Comparative Planetology, Hefei 230026, China

^d Key Laboratory of Space Active Opto-Electronics Technology, Shanghai Institute of Technical Physics, Chinese Academy of Sciences, Shanghai 200083, China

ARTICLE INFO

Article history:

Received 13 November 2019

Received in revised form 17 January 2020

Accepted 21 January 2020

Available online xxx

Editor: F. Moynier

Keywords:

in situ measurements

space weathering

Hapke model

SMFe abundance

Chang'e-4 rover

ABSTRACT

Space weathering introduces confounding effects on visible and near infrared reflectance spectra of airless bodies, which considerably darkens the reflectance, reddens the continuum slope and suppresses absorption features. It's mainly attributed to the gradual formation and accumulation of submicroscopic metallic iron (SMFe) on regolith grains. In situ spectral measurements from Chang'e-4 rover provide a unique opportunity to investigate the space weathering effects on the intact lunar farside regolith. SMFe abundance at the landing site, which is 0.32 ± 0.06 wt.%, is retrieved from in situ measured reflectance spectra by using Hapke model. The derived Is/FeO maturity index (82 ± 15) indicates the Finsen crater ejecta-sourced regolith is mature, which is consistent with the geologic background that it had experienced about 3.7 Ga space weathering.

© 2020 Elsevier B.V. All rights reserved.

1. Introduction

Space weathering is the gradual alteration of materials when they are exposed to a variety of natural processes that occur in the space environment, which is ubiquitous on the Moon and other airless bodies (Pieters and Noble, 2016). The space weathering process results in the visible and near infrared reflectance spectrum of the regolith, which covers many planetary bodies, becomes considerably dark, exhibiting a reddened continuum and even almost completely suppressed absorption features (Pieters and Noble, 2016). The optical effects of space weathering, which has already been successfully simulated in the laboratory (Sasaki et al., 2001; Noble et al., 2007), are mainly caused by the gradual formation and accumulation of submicroscopic metallic iron (SMFe) that imbedded within or deposited on the regolith particles (Pieters et al., 2000; Hapke, 2001; Noble et al., 2001; Lucey and Noble, 2008; Lucey and Riner, 2011). Smaller SMFe particles (<10 nm in diameter) greatly redden spectrum in the visible (VIS) wavelengths while leaving the near-infrared (NIR) region largely unaffected; Larger particles (>40 nm in diameter) darken spectrum across the VIS/NIR range with little change in the overall

shape of the continuum; And intermediate particles impact the spectrum in a distinct pattern that varies with total iron abundance (Noble et al., 2007; Lucey and Noble, 2008). Consequently, the SMFe abundance in the regolith is an important indicator for evaluating space weathering and regolith evolution.

The Moon is a unique body that already has been remotely observed by orbiters, in situ measured by rovers and sampled by manned/unmanned spacecraft. The chemical and spectral data collected during these missions, especially those from the well-studied Apollo and Luna samples, provide valuable and critical ground-truth information to perform quantitative analyses on space weathering from various optical remote sensing techniques, which are the only means to study the vast area of the lunar surface. However, the sampling process may disturb the primitive state of the very top of lunar regolith, the optical properties of returned lunar samples may not be representative of the undisturbed lunar surface (Wang et al., 2017). Sampling the uppermost surface while preserving its structure (e.g. porosity, grain-to-grain contacts) has not been achieved on any sample return mission to date (Noble et al., 2011). Therefore, in situ spectral measurements, along with experiences and expertise from weathering simulation theory (Hapke, 2001; Lucey and Riner, 2011) and practice (Sasaki et al., 2001; Noble et al., 2007), provide a feasible means to study the space weathering effects caused by SMFe on the lunar surface.

* Corresponding author at: P. O. Box 9718, Datun Road, Chaoyang District, Beijing, 100101, China.

E-mail address: dikc@radi.ac.cn (K. Di).

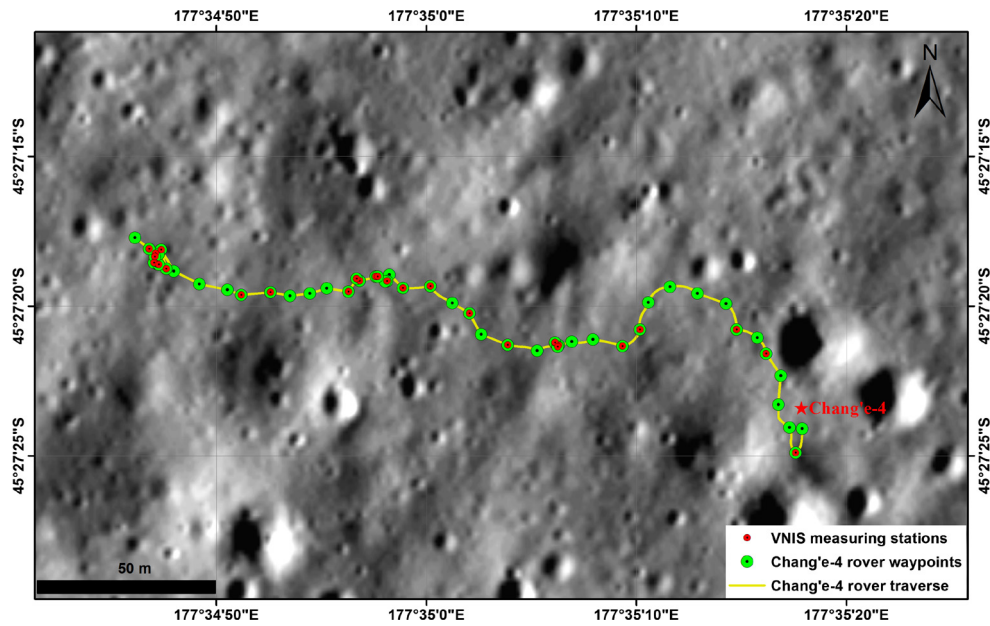


Fig. 1. Traverse map of the Chang'e-4 rover during the first 9 lunar days. The base map is a high resolution (0.9 m/pixel) digital orthophoto map (DOM) (Liu et al., 2019) generated from Lunar Reconnaissance Orbiter Camera (LROC) Narrow Angle Camera (NAC) imagery (Robinson et al., 2010). A detailed regional geologic setting map of the Chang'e-4 landing site is shown in Fig. 3.

China's Chang'e-4 spacecraft successfully landed inside Von Kármán crater within the South Pole-Aitken (SPA) basin on the lunar farside on January 3, 2019 (Di et al., 2019). The Visible and Near-Infrared Imaging Spectrometer (VNIS) (Li et al., 2019), one of the scientific payloads on the deployed Chang'e-4 rover, had made in situ spectral measurements on the lunar regolith along the rover traverse (Fig. 1). These reflectance spectra provide a unique opportunity to investigate the space weathering effects on the intact lunar farside regolith, which is accomplished by evaluating the SMFe abundance via Hapke model (Hapke, 1981; 2001; Lucey and Riner, 2011) in this study.

2. Data

2.1. VNIS spectra

The VNIS instrument consists of a VIS/NIR imager with an effective 256×256 pixels (~ 1 mm/pixel) and a shortwave infrared (SWIR) single-pixel detector (Li et al., 2019). The VIS/NIR imager works from 450 to 945 nm with a spectral resolution of 2–7 nm, and the SWIR detector works from 900 to 2,395 nm with a spectral resolution of 3–12 nm (Li et al., 2019). The VNIS made in situ measurements on the lunar regolith along the traverse at different stations between the first and the ninth lunar days (January 3 – September 6, 2019). These measured raw data are preprocessed and released to the scientific team members as L2B radiance spectra by the team of ground application and research system (GRAS). The L2B radiance spectra are further processed in this study by the solar irradiance calibration method (Gou et al., 2019) to derive full-range reflectance spectra to study the space weathering effects (Fig. 2).

Indoor radiance calibration at typical temperature (20 °C) shows the signal-to-noise ratio (SNR) values of VNIS are greater than 50 dB in the wavelength range of 1000 nm to 2200 nm (He et al., 2019). Inflight radiance calibration shows that the SNR values are greater than 40 dB in the wavelength range of 1200 nm to 2400 nm. On one hand, averaging is an effective way to improve SNR, and the SNR values of the VNIS at VIS/NIR wavelengths shown in both He et al. (2019) and Li et al. (2019) were calculated by averaging the pixels within the field of view of SWIR, however the

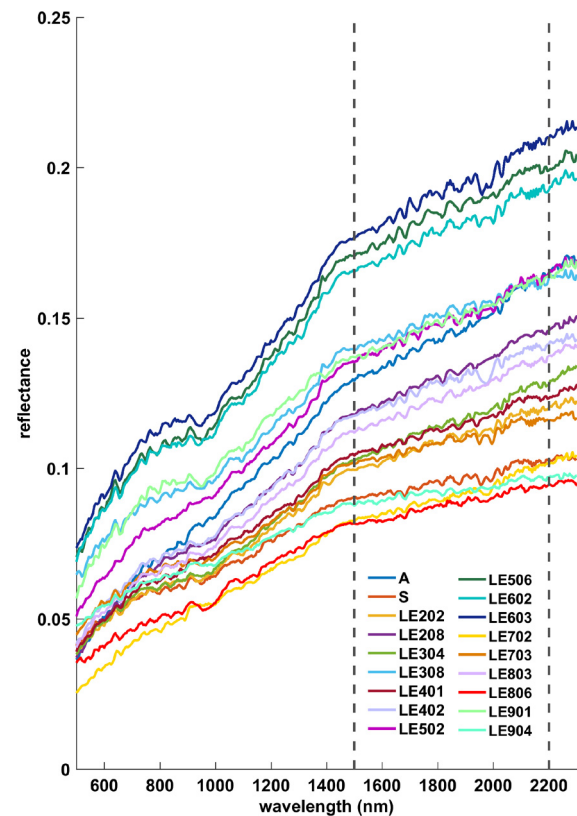


Fig. 2. Examples of in situ measured VNIS spectra on the lunar regolith at different rover stations. Only two of the multiple spectra measured in each lunar day are shown here. For example, spectra A and S are measured during the first lunar day. All the spectra analyzed in this study are shown in the supplementary material. The dashed lines located at 1500 nm and 2200 nm mark the wavelength range used for simulation in this study to avoid thermal emission effects at longer wavelengths (Li and Milliken, 2016) and low signal-to-noise ratio (SNR) at shorter wavelengths (He et al., 2019; Li et al., 2019). (For interpretation of the colors in the figure(s), the reader is referred to the web version of this article.)

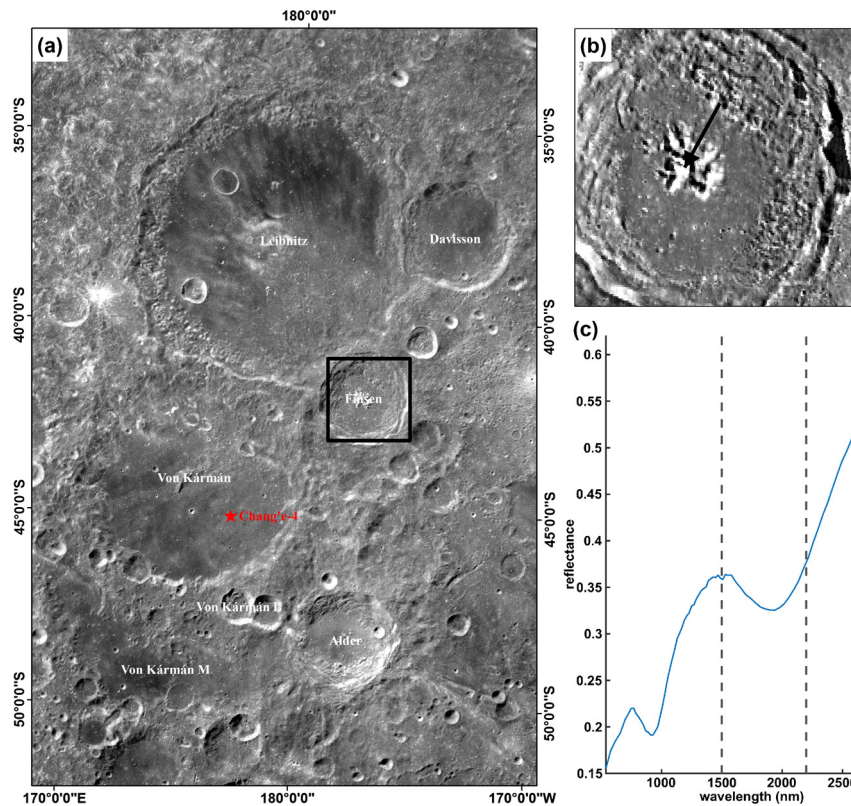


Fig. 3. (a) Chang'e-2 image (Ren et al., 2014) of Chang'e-4 landing site inside the Von Kármán crater and surrounding craters. (b) M^3 reflectance image @750 nm of Finsen crater, with location indicated by the black box in (a) (image ID: M3G20090815T202602); (c) M^3 spectrum corresponding to the central peak of Finsen crater, with location indicated by the black arrow in (b). The spectrum is derived from a 3×3 pixel average.

SNR values of VIS/NIR are still lower than that of SWIR. On the other hand, due to the design principle of the VNIS instrument (He et al., 2019), in situ measured spectrum may have a spectral kink around 1400 nm. Therefore, VNIS spectra from 1500 nm to 2200 nm are used in this study to avoid the thermal emission effects at longer wavelengths (Li and Milliken, 2016) and low SNR at shorter wavelengths (He et al., 2019; Li et al., 2019).

2.2. Moon Mineralogy Mapper spectrum

The Moon Mineralogy Mapper (M^3), flew aboard India's Chandrayaan-1, is a push-broom imaging spectrometer that operates from the visible into the near infrared (0.42–3.0 μm). M^3 observes the lunar surface in a high-resolution targetmode (80 m/pixel; 260 spectral channels), or in a low-resolution global mode (140 m/pixel; 85 spectral channels) (Pieters et al., 2009). The M^3 Level 2 spectral reflectance image (REFIMG) is used in this study, which consists of photometrically calibrated reflectance data that has been corrected for thermal emission (Clark et al., 2011; Besse et al., 2013).

Numerical simulations suggested that the SPA basin-forming event should have sampled the lunar lower crust and upper mantle (Miljkovic et al., 2015; Melosh et al., 2017). The event could generate an impact melt pool with a radius of about 200 km and a depth of approximately 50 km within the basin (Hurwitz and Kring, 2014; Vaughan and Head, 2014). The melt was initially relatively homogeneous because of the thorough mixing, however, it had differentiated to form shallow noritic layers with a thickness of ~ 6 km (Hurwitz and Kring, 2014). Studies revealed that the regolith observed by the Chang'e-4 rover was sourced from Finsen crater ejecta (Huang et al., 2018; Di et al., 2019). The 3.9-km-deep Finsen crater (42.29° S, 177.72° W, diameter = 73 km)

is a well-preserved complex crater that has a prominent central peak. The estimated transient cavity radius of the SPA basin ranges from 840 km to 1400 km (Spudis et al., 1994; Petro and Pieters, 2002; Potter et al., 2012). Finsen crater is just 370 km away from the center of the SPA basin. The estimated approximate maximum excavation depth H_{exc} of Finsen crater, which can be calculated from $H_{exc} \approx 0.05 - 0.065D$ (D is the final complex crater diameter) (Melosh, 1989), is about 3.65–4.74 km. Therefore, the Finsen crater ejecta were very likely completely sourced from the shallow noritic layers. In this case, the shallower material that was ejected from the Finsen crater and the relative deeper material in the central peak would have the same composition. The central peak bedrock of Finsen crater has steep walls that prevent the accumulation of a space-weathered regolith layer, thus preserves optical immaturity (Tompkins and Pieters, 1999). A large portion of the ejecta was from the excavated material during the crater formation, hence, M^3 spectrum of the exposed central peak of Finsen crater, which is resampled to the VNIS bands to ensure both have the same spectral resolution (band number), is used as the base spectrum in this study. The spectrum clearly exhibits strong mafic absorptions at short wavelengths, indicating the relatively pristine state (optical immaturity) was kept since the central peak formed and the presence of Mg-rich low-Ca pyroxene (LCP) (Fig. 3).

3. Quantifying SMFe abundance in lunar regolith

Hapke model (Hapke, 1981; 2001; Lucey and Riner, 2011) is used in this study to quantify the SMFe mass fraction in the lunar regolith at Chang'e-4 landing site from in situ measured VNIS spectra. Details of assessing the SMFe abundance are described below.

3.1. Single scattering albedo determination

With the assumptions that all materials within the media are mixed intimately and the particle size is much larger than the spectral wavelength, Hapke model (Hapke, 1981) offers an approximate solution to the radiative transfer theory to derive bidirectional reflectance r (equation (1)). However, reflectance factor (REFF) is derived from VNIS calibrated radiance by the solar irradiance calibration method in this study (Gou et al., 2019). The reflectance factor REFF is related to the bidirectional reflectance r by equation (2). Hence, the relationship between reflectance factor REFF and single-scattering albedo can be expressed in equation (3).

$$r(i, e, g) = \frac{\omega_{avg}}{4\pi} \frac{\mu_0}{(\mu_0 + \mu)} [(1 + B(g))P(g) + H(\mu_0, \omega_{avg})H(\mu, \omega_{avg}) - 1] \quad (1)$$

$$REFF = \frac{\pi * r}{\mu_0} \quad (2)$$

$$REFF(i, e, g) = \frac{\omega_{avg}}{4(\mu_0 + \mu)} [(1 + B(g))P(g) + H(\mu_0, \omega_{avg})H(\mu, \omega_{avg}) - 1] \quad (3)$$

where μ_0 and μ are the cosine of the incidence angle i and emission (viewing) angle e , respectively; g is phase angle. ω_{avg} is the average single scattering albedo (SSA) of all the components. $B(g)$ is the backscatter function that describes opposition effect (equation (4)). $P(g)$ is the single-particle phase function, which can be approximated by a second-order Legendre polynomial series (equation (6)). $H(x, \omega_{avg})$ is the isotropic scattering function approximation (equation (7)) (Hapke, 2002).

$$B(g) = \frac{B_0}{1 + (1/h) \tan(g/2)} \quad (4)$$

where B_0 is the amplitude of the opposition effect (set to 1 in this study) (Hapke, 1981), and h is the angular width parameter of the opposition effect, which is approximated by equation (5).

$$h = -\frac{3}{8} \ln(1 - \varphi) \quad (5)$$

where φ is the filling factor (decreasing porosity), which is set to 0.41 for lunar regolith (Bowell et al., 1989).

$$P(g) = 1 + b \cos(g) + c(1.5 \cos^2(g) - 0.5) \quad (6)$$

b and c are set to -0.4 and 0.25 , respectively (Mustard and Pieters, 1989).

$$H(x, \omega_{avg}) = \left[1 - \omega x \left[r_0 + \frac{1 - 2r_0 x}{2} \ln \left(\frac{1 + x}{x} \right) \right] \right]^{-1} \quad (7)$$

$$\text{where } r_0 = \frac{1 - \sqrt{1 - \omega_{avg}}}{1 + \sqrt{1 - \omega_{avg}}}$$

When equations (4)–(7) are inserted into equation (3), a nonlinear relationship between REFF and ω_{avg} can be established. Therefore, the average single scattering albedo ω_{avg} of the lunar regolith at Chang'e-4 landing site can be solved from the in situ measured VNIS reflectance spectrum.

3.2. Absorption coefficient determination

Theoretically, ω_{avg} can be computed by equation (8) (Hapke, 2012).

$$\omega_{avg} = S_e + (1 - S_e) \frac{(1 - S_i)\Theta}{1 - S_i\Theta} \quad (8)$$

where S_e and S_i are the average Fresnel reflection coefficients for externally and internally incident light, respectively. Θ is the internal transmission coefficient of the particle without internal scatters. S_e and S_i are empirically approximated by equations (9) and (10) (Hapke, 2012). Θ is calculated from equation (12).

$$S_e = 0.0587 + 0.8453R(0) + 0.08707R(0)^2 \quad (9)$$

$$S_i = 1 - \frac{1}{n^2} [0.9413 - 0.8453R(0) + 0.08707R(0)^2] \quad (10)$$

$$R(0) = [(n - 1)^2 + k^2] / [(n + 1)^2 + k^2] \quad (11)$$

where n and k are the real part (refractive index) and imagery part (extinction coefficient) of the complex refractive index (also known as optical constant), respectively. For the lunar regolith, the refractive index n is 1.78 (Hapke, 1994).

$$\Theta = e^{-\alpha < D >} \quad (12)$$

where α is the absorption coefficient, $\langle D \rangle$ is the average distance traveled by all rays during a single transit of the particle, which has various approximation expressions (Hapke, 2001). Area weighted mean size (equation (13)) is adopted in this study

$$\langle D \rangle = D_L \ln \frac{D_U}{D_L} \quad (13)$$

where D_U and D_L are the effective upper and lower limit of the particle size. As for the Apollo lunar regolith sample, the effective upper and lower limit of the mineral particle sizes are 1000 μm and 5 μm , hence the approximate effective optical path is about 26 μm and this value is adopted for deriving absorption coefficient from SSA in this study.

When equation (12) is inserted into equation (8), the relationship between absorption coefficient of the lunar regolith α and average single scattering albedo ω_{avg} can be expressed in equation (14).

$$\alpha = \frac{1}{\langle D \rangle} \ln \left[S_i + \frac{(1 - S_e)(1 - S_i)}{\omega_{avg} - S_e} \right] \quad (14)$$

3.3. Space weathering simulation

Assuming the space weathering being proportional to the mass fraction of SMFe, Hapke (2001) successfully re-produced the reddening and darkening effects caused by fine-grained SMFe particles, Lucey and Riner (2011) proposed a new formulation to model the effects of particles at any size by using Mie theory (equation (15)).

$$\alpha_w = \alpha_h + \alpha_g + \alpha_c \quad (15)$$

where α_w and α_h are the absorption coefficients of the weathered host material and unweathered host material (equation (14)), respectively; α_g and α_c represent the additional absorption due to SMFe within grains (equation (16)) and in coatings (equation (17)), respectively.

$$\alpha_g = \frac{36\pi M_g \rho_h}{\lambda \rho_{Fe}} \cdot \frac{n_h^3 n_{Fe} k_{Fe}}{(n_{Fe}^2 - k_{Fe}^2 + 2n_h^2)^2 + 4n_{Fe}^2 k_{Fe}^2} \quad (16)$$

$$\alpha_c = \frac{36\pi M_c \rho_h}{\lambda \rho_{Fe}} \cdot \frac{n_h^3 n_{Fe} k_{Fe}}{(n_{Fe}^2 - k_{Fe}^2 + 2n_h^2)^2 + 4n_{Fe}^2 k_{Fe}^2} \quad (17)$$

where M_g and M_c are the mass fraction of SMFe in the grain and coating relative to the host material. λ is wavelength; n_* , k_* , ρ_* ($*$ denotes h or Fe) are the real and imagery parts of the complex refractive index, and density of host material or SMFe, respectively.

The optical constants of *Fe* used in this study are from Query (1985).

The REFF spectrum with different mass fraction of SMFe incorporated on the host material can thus be simulated by inserting equation (15) into (8), and then into (3).

3.4. SMFe abundance estimation

The mass fraction of SMFe in the lunar regolith is estimated by comparing the spectral shape similarity between in situ measured VNIS spectrum and simulated M^3 spectrum by considering the contribution of SMFe. The simulated M^3 spectrum is created by adding various amounts of SMFe (0.0–2.0 wt.%) with an increment of 0.001 wt.%. The similarity between these two spectra is measured through the spectral angle parameter θ (in radians) by spectral angle mapper (SAM) technique (equation (18)) (Kruse et al., 1993). Smaller angles indicate higher similarity between the in situ measured VNIS spectrum and the simulated M^3 spectrum. The reason for choosing SAM technique is that it concentrates on spectral shape and is insensitive to absolute reflectance related to illumination or albedo effects. As stated in the section 2.1, the comparison is performed over the wavelength range 1500–2200 nm in this study to avoid the thermal emission effects at longer wavelengths (Li and Milliken, 2016) and low SNR at shorter wavelengths (He et al., 2019; Li et al., 2019). The optimal estimation for the mass fraction of SMFe in the lunar regolith at Chang'e-4 landing site is determined when the spectral angle between the in situ measured VNIS spectrum and the simulated M^3 spectrum becomes the lowest.

$$\theta = \cos^{-1} \left(\frac{\sum_{\lambda=1}^N \text{REFF}_{\lambda} \text{REFF}'_{\lambda}}{\sqrt{\sum_{\lambda=1}^N \text{REFF}_{\lambda}^2} \sqrt{\sum_{\lambda=1}^N \text{REFF}'_{\lambda}^2}} \right) \quad (18)$$

where REFF_{λ} and REFF'_{λ} ($\lambda = 1, 2, \dots, N$) are the in situ measured VNIS spectrum and simulated M^3 spectrum, respectively.

4. Result and discussion

4.1. SMFe abundance

The method used in this study successfully simulates the spectral shape of the in situ measured VNIS spectrum from the base M^3 spectrum. For example, the best match for a regolith spectrum measured by VNIS at station LE902 is found to be the M^3 spectrum plus 0.42 wt.% SMFe (Supplementary Fig. 1), which is typical for mature lunar regolith (Warell and Blewett, 2004). The average SMFe abundance in the lunar regolith at Chang'e-4 landing site, which is derived from 34 in situ measured spectra, is 0.32 ± 0.06 wt.%. Trang and Lucey (2019) produced a SMFe abundance map through radiative transfer modeling of Kaguya multi-band imager (MI) data. The SMFe abundance at Chang'e-4 landing site reported in their work is about 1.31 wt.%, which is the sum of the nanophase (particles <100 nm in diameter) and microphase iron (particles >100 nm in diameter) abundances. The possible main reason for the discrepancy is that the SMFe particles in the regolith at Chang'e-4 landing site may be chiefly in nanophase form. In this scenario, the slight difference between the estimated SMFe abundance (~ 0.32 wt.%) in this study and the nanophase iron abundance (~ 0.43 wt.%) reported by Trang and Lucey (2019) may attributed to: (1) different observation modes, i.e., in situ observation for the VNIS and orbital observation for the MI. (2) huge resolution differences, i.e., ~ 1 mm/pixel from a detection distance of 1 m for the VNIS and ~ 30.3 km/pixel for the reported map. Wang et al. (2017) estimated the SMFe abundance

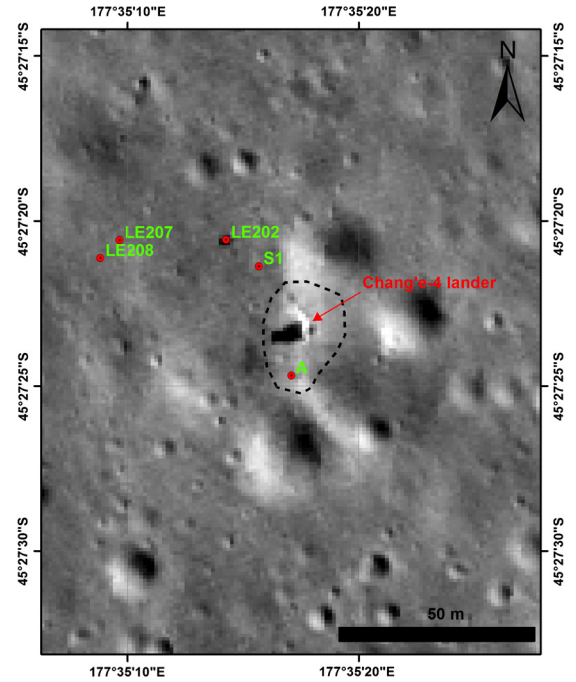


Fig. 4. The region severely affected by rocket engine plume during soft landing. It is outlined by the black dotted line and is about 450 m² (LROC NAC image ID: M1303619844LE).

(0.368 wt.%) and inferred the regolith at Chang'e-3 landing site to be submature after analyzing a spectrum measured by VNIS on the minimally disturbed regolith at Chang'e-3 landing site (Mare Imbrium). Although the regoliths at Chang'e-3 and Chang'e-4 landing sites have similar SMFe abundance, the SMFe saturation limit generally increases with FeO content (Trang and Lucey, 2019), which is important for estimating the maturity degree. The FeO contents at Chang'e-3 and Chang'e-4 landing sites are ~ 22.8 wt.% (Ling et al., 2015) and ~ 12.6 wt.% (Supplementary Fig. 2), respectively. The absolute model ages of the two landing sites are 27–80 Ma (Xiao et al., 2015) and 3.7 Ga (Supplementary Text 1), respectively. Considering the large differences in both FeO content and absolute model age between the two landing sites, the lunar regolith maturity degree at Chang'e-4 landing site is mature (discussed in the next section) and different from that at Chang'e-3 landing site.

By comparing images acquired both before and after the Chang'e-4 probe landing by the LROC NAC, it is found that the lander rocket plume had modified the surface. This effect had also been observed in previous missions (Clegg et al., 2014). The severely affected region, which was disturbed by Chang'e-4 probe descent engine during soft landing, is approximately 450 m² (Fig. 4). The rover station A, which has an abundance of 0.27 wt.% and is about 12.9 m from the lander, is within the most significantly affected region. Because rocket plume can blow away the very uppermost, finest, and highly mature particles, previous study reported that the SMFe abundance in the regolith may vary significantly with distance from the lander (Wang et al., 2017). However, the phenomenon is not observed at Chang'e-4 landing site. For example, the VNIS made in situ measurements sequentially at rover stations S1, LE202, LE207 and LE208 just immediately after station A (Fig. 4). These stations are not within the extent of the possible severely affected region, and they are 19.2 m, 28.6 m, 50.6 m and 53.5 m away from the lander. The SMFe abundances estimated from VNIS spectra at these stations are 0.34 wt.%, 0.30 wt.%, 0.27 wt.% and 0.28 wt.%, respectively (Supplementary Fig. 1). The possible reason for the insignificant SMFe abundance difference is that the relative high regolith growth rate (3.1 m/Gyr) at Chang'e-4 landing area (Lai et al., 2019). The fast gardening and impacting

processes that formed the regolith had sufficiently mixed the uppermost, finest, and highly mature particles.

4.2. Regolith maturity

Morris (1980) deduced the relationship between SMFe abundance, FeO content, and maturity index Is/FeO from Apollo and Lunar regolith samples, and classified the regolith into three categories: immature ($0.0 < Is/FeO < 29.0$), submature ($30.0 < Is/FeO < 59.0$), mature ($Is/FeO > 60.0$). According to the products derived from Kaguya lunar multiband imager (Lemelin et al., 2016), the FeO abundance at Chang'e-4 landing site (Supplementary Fig. 2) is 12.6 ± 0.6 wt.%. Hence, the calculated Is/FeO value is 82 ± 15 , indicating the regolith at Chang'e-4 landing site is mature. As noted by Wang et al. (2017), the ferromagnetic resonance technique used by Morris (1980) to determine the Is value is only sensitive to iron particles in the diameter range about 4–33 nm. However, the influence of SMFe particles >33 nm, which are not sensed by magnetic resonance, is taken into consideration (equation (15)) by the spectral simulation process in this study. As a result, the use of estimated SMFe abundance in this study tends to slightly overestimate the Is/FeO value. However, it should be noted that the SMFe content of the base M^3 spectrum of the central peak bedrock is assumed to be zero, which can cause an underestimation because of the existence of possible little patina on the surface of the rock. Consequently, the overestimation of Is/FeO value should be balanced to some extent by the underestimation of SMFe content in the base M^3 spectrum.

The maturity of lunar regolith is a function of weathering environment, surface properties, exposure time, and gardening rates (Pieters and Noble, 2016). To simplify the actual dynamic space weathering process, assume the lunar regolith at Chang'e-4 landing site accumulated SMFe immediately and steadily after its formation, thus the maturity index Is/FeO can be treated as an indicator of exposure age to the harsh space environment. For example, radiometric dating revealed that many of the Apollo 17 samples are 3.6–4.2 billion years old, and Is/FeO values indicate they are mature (e.g., 93 for sample 78221, 82 for sample 72150) (Morris, 1978). The Von Karman crater was formed about 3.97 billion years ago (Yingst et al., 2017), and Finsen crater ejecta that had covered/sculptured the crater floor mare plain at the landing site happened around 3.7 billion years ago (Supplementary Text 1). Hence, the high Is/FeO of the regolith at the Chang'e-4 landing site is generally consistent with the geologic background that the regolith had experienced 3.7 billion years of space weathering.

5. Conclusion

Chang'e-4 rover made in situ spectral measurements on the lunar farside regolith, which provides a unique chance to study space weathering effects on an airless planetary body. In order to simulate the space weathering effects that arise from SMFe in the visible and the near infrared region, i.e., reflectance darkening, continuum slope reddening and absorption features flattening, Hapke model is used in this study to investigate the SMFe abundance in the regolith at the Chang'e-4 landing site. Simulation results reveal that the average SMFe abundance in the regolith is 0.32 ± 0.06 wt.%. The derived Is/FeO maturity index, which is 82 ± 15 , indicates the regolith at Chang'e-4 landing site is mature. The mature state is consistent with the geologic background that the Finsen crater ejecta-sourced regolith, which was measured by Chang'e-4 rover, had experienced about 3.7 billion years space weathering that caused by solar wind, galactic cosmic rays, micrometeorites and larger meteors.

Declaration of competing interest

The authors declare that they have no known competing financial interests or personal relationships that could have appeared to influence the work reported in this paper.

Acknowledgements

The authors gratefully thank the whole Chang'e-4 team for making the mission a great success and providing the data (<http://moon.bao.ac.cn/>). This research is supported by the B-type Strategic Priority Program of the Chinese Academy of Sciences (grant No. XDB41000000), National Natural Science Foundation of China (grant Nos. 41702354 and 41941003), Macau Young Scholars Program (grant No. AM201902), and Science and Technology Development Fund of Macau (grant No. 131/2017/A3). Constructive reviews by anonymous reviewers improved the quality of this manuscript substantially, and are greatly appreciated.

Appendix A. Supplementary material

Supplementary material related to this article can be found online at <https://doi.org/10.1016/j.epsl.2020.116117>.

References

- Besse, S., Yokota, Y., Boardman, J., Green, R., Haruyama, J., Isaacson, P., Mall, U., Matsunaga, T., Ohtake, M., Pieters, C., Staid, M., Sunshine, J., Yamamoto, S., 2013. One Moon, many measurements 2: photometric corrections. *Icarus* 226, 127–139.
- Bowell, E., Hapke, B., Domingue, D., Lumme, K., Peltoniemi, J., Harris, A., 1989. Application of photometric models to asteroids. In: Binzel, R.P., Gehrels, T., Shapley Matthews, M. (Eds.), *Asteroids II*. The University of Arizona Press, Tucson, AZ, pp. 524–556.
- Clark, R.N., Pieters, C.M., Green, R.O., Boardman, J.W., Petro, N.E., 2011. Thermal removal from near-infrared imaging spectroscopy data of the Moon. *J. Geophys. Res.*, Planets 116, E00G16.
- Clegg, R.N., Jolliff, B.L., Robinson, M.S., Hapke, B.W., Plescia, J.B., 2014. Effects of rocket exhaust on lunar soil reflectance properties. *Icarus* 227, 176–194.
- Di, K., Zhu, M.-H., Yue, Z., Lin, Y., Wan, W., Zhaoqin, Liu, Gou, S., Liu, B., Man, Peng, Wang, Y., Niu, S., Zhang, J., Li, J., Xie, J., Xi, L., Yang, J., Xue, B., 2019. Topographic evolution of Von Kármán crater revealed by the lunar rover Yutu-2. *Geophys. Res. Lett.* 46, 12764–12770.
- Gou, S., Di, K., Yue, Z., Liu, Z., He, Z., Xu, R., Lin, H., Liu, B., Peng, M., Wan, W., Wang, Y., Liu, J., 2019. Lunar deep materials observed by Chang'e-4 rover. *Earth Planet. Sci. Lett.* 528, 115829.
- Hapke, B., 1981. Bidirectional reflectance spectroscopy: 1. Theory. *J. Geophys. Res.*, Solid Earth 86, 3039–3054.
- Hapke, B., 1994. The refractive index of the regolith of mercury. In: 25th Lunar and Planetary Science Conference. Houston, TX, pp. 507–508.
- Hapke, B., 2001. Space weathering from Mercury to the asteroid belt. *J. Geophys. Res.* 106, 10039–10073.
- Hapke, B., 2002. Bidirectional reflectance spectroscopy: 5. The coherent backscatter opposition effect and anisotropic scattering. *Icarus* 157, 523–534.
- Hapke, B., 2012. *Theory of Reflectance and Emittance Spectroscopy*, second edition. Cambridge University Press, Cambridge.
- He, Z., Li, C., Xu, R., Lv, G., Yuan, L., Wang, J., 2019. Spectrometers based on acousto-optic tunable filters for in-situ lunar surface measurement. *J. Appl. Remote Sens.* 13, 027502.
- Huang, J., Xiao, Z., Flahaut, J., Martinot, M., Head, J., Xiao, X., Xie, M., Xiao, L., 2018. Geological characteristics of Von Kármán Crater, Northwestern South Pole-Aitken Basin: Chang'E-4 landing site region. *J. Geophys. Res.*, Planets 123, 1684–1700.
- Hurwitz, D.M., Kring, D.A., 2014. Differentiation of the South Pole–Aitken basin impact melt sheet: implications for lunar exploration. *J. Geophys. Res.*, Planets 119, 1110–1133.
- Kruse, F., Lefkoff, A., Boardman, J., Heidebrecht, K., Shapiro, A., Barloon, P., Goetz, A., 1993. The spectral image processing system (SIPS)—interactive visualization and analysis of imaging spectrometer data. *Remote Sens. Environ.* 44, 145–163.
- Lai, J., Xu, Y., Zhang, X., Xiao, L., Yan, Q., Meng, X., Zhou, B., Dong, Z., Zhao, D., 2019. Comparison of dielectric properties and structure of lunar regolith at Chang'e-3 and Chang'e-4 landing sites revealed by ground penetrating radar. *Geophys. Res. Lett.* 46, 12783–12793. <https://doi.org/10.1029/2019GL084458>.
- Lemelin, M., Lucey, P.G., Gaddis, L.R., Hare, T., Ohtake, M., 2016. Global map products from the Kaguya Multiband Imager at 512 ppd: minerals, FeO and OMAT. In: 47th Lunar and Planetary Science Conference. Lunar and Planetary Institute, The Woodlands, Texas, p. 2994.

- Li, S., Milliken, R.E., 2016. An empirical thermal correction model for Moon Mineralogy Mapper data constrained by laboratory spectra and Diviner temperatures. *J. Geophys. Res., Planets* 121, 2081–2107.
- Li, C.L., Xu, R., Lv, G., Yuan, L.Y., He, Z.P., Wang, J.Y., 2019. Detection and calibration characteristics of the visible and near-infrared imaging spectrometer in the Chang'e-4. *Rev. Sci. Instrum.* 90, 103106.
- Ling, Z., Jolliff, B.L., Wang, A., Li, C., Liu, J., Zhang, J., Li, B., Sun, L., Chen, J., Xiao, L., Liu, J., Ren, X., Peng, W., Wang, H., Cui, X., He, Z., Wang, J., 2015. Correlated compositional and mineralogical investigations at the Chang'e-3 landing site. *Nat. Commun.* 6, 8880.
- Liu, B., Niu, S., Xin, X., Jia, M., Di, K., Liu, Z., Peng, M., Yue, Z., 2019. High precision DTM and DOM generating using multi-source orbital data on Chang'e-4 landing site. In: *Int. Arch. Photogramm. Remote Sens. Spatial Inf. Sci. Copernicus Publications*, Enschede, the Netherlands, pp. 1413–1417.
- Lucey, P.G., Noble, S.K., 2008. Experimental test of a radiative transfer model of the optical effects of space weathering. *Icarus* 197, 348–353.
- Lucey, P.G., Riner, M.A., 2011. The optical effects of small iron particles that darken but do not redden: evidence of intense space weathering on Mercury. *Icarus* 212, 451–462.
- Melosh, H.J., 1989. *Impact Cratering: A Geologic Process*. Oxford University Press.
- Melosh, H.J., Kendall, J., Horgan, B., Johnson, B.C., Bowling, T., Lucey, P.G., Taylor, G.J., 2017. South Pole–Aitken basin ejecta reveal the Moon's upper mantle. *Geology* 45, 1063–1066.
- Miljkovic, K., Wieczorek, M.A., Collins, G.S., Solomon, S.C., Smith, D.E., Zuber, M.T., 2015. Excavation of the mantle in basin-forming events on the Moon. *Earth Planet. Sci. Lett.* 409, 243–251.
- Morris, R.V., 1978. The surface exposure (maturity) of lunar soils: some concepts and IS/FeO compilation. In: *9th Lunar and Planetary Science Conference*. Pergamon Press, Houston, TX, pp. 2287–2297.
- Morris, R.V., 1980. Origins and size distribution of metallic iron particles in the lunar regolith. In: *11th Lunar and Planetary Science Conference*. Pergamon Press, Houston, TX, pp. 1697–1712.
- Mustard, J.F., Pieters, C.M., 1989. Photometric phase functions of common geologic minerals and applications to quantitative analysis of mineral mixture reflectance spectra. *J. Geophys. Res., Solid Earth* 94, 13619–13634.
- Noble, S.K., Keller, L.P., Christoffersen, R., 2011. Sampling the uppermost surface of airless bodies. In: *The Importance of Solar System Sample Return Missions to the Future of Planetary Science*. The Woodlands, Texas, p. 5008.
- Noble, S.K., Pieters, C.M., Keller, L.P., 2007. An experimental approach to understanding the optical effects of space weathering. *Icarus* 192, 629–642.
- Noble, S., Pieters, C., Taylor, L., Morris, R., Allen, C., McKay, D., Keller, L., 2001. The optical properties of the finest fraction of lunar soil: implications for space weathering. *Meteorit. Planet. Sci.* 36, 31–42.
- Petro, N.E., Pieters, C.M., 2002. The size and location of the transient crater of the South Pole–Aitken basin. In: *33rd Lunar and Planetary Science Conference*. Houston, Texas, p. 1848.
- Pieters, C.M., Boardman, J., Buratti, B., Chatterjee, A., Clark, R., Glavich, T., Green, R., Head, J., Isaacson, P., Malaret, E., 2009. The Moon mineralogy mapper (M3) on Chandrayaan-1. *Curr. Nanosci.* 96, 500–505.
- Pieters, C.M., Noble, S.K., 2016. Space weathering on airless bodies. *J. Geophys. Res., Planets* 121, 1865–1884.
- Pieters, C.M., Taylor, L.A., Noble, S.K., Keller, L.P., Hapke, B., Morris, R.V., Allen, C.C., McKay, D.S., Wentworth, S., 2000. Space weathering on airless bodies: resolving a mystery with lunar samples. *Meteorit. Planet. Sci.* 35, 1101–1107.
- Potter, R.W.K., Collins, G.S., Kiefer, W.S., McGovern, P.J., Kring, D.A., 2012. Constraining the size of the South Pole–Aitken basin impact. *Icarus* 220, 730–743.
- Querry, M.R., 1985. *Optical Constants*. Contractor Report CRDC-CR-85034.
- Ren, X., Liu, J.J., Wang, F.F., Wang, W.R., Mu, L.L., Li, H.H., 2014. A new lunar global topographic map products from Chang'E-2 stereo camera image data. In: *European Planetary Science Congress*. Centro de Congressos do Estoril, Cascais, Portugal, pp. EPSC2014–EPSC2344.
- Robinson, M.S., Brylow, S.M., Tschimmel, M., Humm, D., Lawrence, S.J., Thomas, P.C., Denevi, B.W., Bowman-Cisneros, E., Zerr, J., Ravine, M.A., Caplinger, M.A., Ghaemi, F.T., Schaffner, J.A., Malin, M.C., Mahanti, P., Bartels, A., Anderson, J., Tran, T.N., Eliason, E.M., McEwen, A.S., Turtle, E., Jolliff, B.L., Hiesinger, H., 2010. Lunar Reconnaissance Orbiter Camera (LROC) instrument overview. *Space Sci. Rev.* 150, 81–124.
- Sasaki, S., Nakamura, K., Hamabe, Y., Kurahashi, E., Hiroi, T., 2001. Production of iron nanoparticles by laser irradiation in a simulation of lunar-like space weathering. *Nature* 410, 555–557.
- Spudis, P.D., Gillis, J.J., Reisse, R.A., 1994. Ancient multiring basins on the Moon revealed by Clementine laser altimetry. *Science* 266, 1848–1851.
- Tompkins, S., Pieters, C.M., 1999. Mineralogy of the lunar crust: results from Clementine. *Meteorit. Planet. Sci.* 34, 25–41.
- Trang, D., Lucey, P.G., 2019. Improved space weathering maps of the lunar surface through radiative transfer modeling of Kaguya multiband imager data. *Icarus* 321, 307–323.
- Vaughan, W.M., Head, J.W., 2014. Impact melt differentiation in the South Pole–Aitken basin: some observations and speculations. *Planet. Space Sci.* 91, 101–106.
- Wang, Z., Wu, Y., Blewett, D.T., Cloutis, E.A., Zheng, Y., Chen, J., 2017. Submicroscopic metallic iron in lunar soils estimated from the in situ spectra of the Chang'E-3 mission. *Geophys. Res. Lett.* 44, 3485–3492.
- Warell, J., Blewett, D.T., 2004. Properties of the Hermean regolith: V. New optical reflectance spectra, comparison with lunar anorthosites, and mineralogical modelling. *Icarus* 168, 257–276.
- Xiao, L., Zhu, P., Fang, G., Xiao, Z., Zou, Y., Zhao, J., Zhao, N., Yuan, Y., Qiao, L., Zhang, X., Zhang, H., Wang, J., Huang, J., Huang, Q., He, Q., Zhou, B., Ji, Y., Zhang, Q., Shen, S., Li, Y., Gao, Y., 2015. A young multilayered terrane of the northern Mare Imbrium revealed by Chang'E-3 mission. *Science* 347, 1226–1229.
- Yingst, R.A., Chuang, F.C., Berman, D.C., Mest, S.C., 2017. Geologic mapping of the Planck quadrangle of the Moon (LQ-29). In: *48th Lunar and Planetary Science Conference*. The Woodlands, Texas, p. 1680.